Global modelling studies of composition and decadal trends of the Asian Tropopause Aerosol Layer

Adriana Bossolasco[1], Fabrice Jegou[1], Pasquale Sellitto[2], Gwenaël Berthet[1], Corinna Kloss[1], and Bernard Legras[3]

[1]Laboratoire de Physique et Chimie de l'Environnement et de l'Espace, CNRS/Université d'Orléans, UMR 7328, Orléans, France
[2]Laboratoire Interuniversitaire des Systèmes Atmosphériques, UMR CNRS 7583, IPSL, Université Paris-Est Créteil/Université de Paris, Créteil, France
[3]Laboratoire de Météorologie Dynamique, UMR CNRS 8539, IPSL, ENS-PSL/Sorbonne Université//École Polytechnique, Paris, France

Correspondence to: Adriana Bossolasco (adriana.bossolasco@cnrs-orleans.fr)

Abstract. The Asian Summer Monsoon (ASM) traps convectively-lifted boundary layer pollutants inside its upper-tropospheric lower-stratospheric Asian monsoon anticyclone (AMA). It is associated with a seasonal and spatially-confined enhanced aerosol layer, called the Asian Tropopause Aerosol Layer (ATAL). The knowledge of the ATAL properties in terms of aerosol budget, chemical composition, as well as its variability and temporal trend is still largely uncertain, due to the dynamical variability of the AMA, the dearth of in situ observations in this region, the complex transport pathways of pollutants and its atmospheric chemical processes. In this work, we use the Community Earth System Model (CESM 1.2 version) based on the coupling of the Community Atmosphere Model (CAM5) and the MAM7 (Modal Aerosol Model) aerosol module to simulate the composition of the ATAL and its decadal trends. Our simulations cover a long-term period of 16 years from 2000 to 2015. We identify a "double-peak" aerosols vertical profile for the ATAL. We attribute the upper peak (around 100 hPa, predominant during early ATAL in June) to dry aerosols, possibly from nucleation processes and the lower peak (around 250 hPa, predominant for a well-developed and late ATAL, in July and August) to cloud-borne aerosols associated with convective clouds. We find that mineral dust is the dominant aerosol by mass in the ATAL showing a large interannual variability, but no long-term trend, due to its natural variation. The results between 120-80 hPa (dry aerosol peak) suggest that for aerosols other than dust the ATAL is composed of around 40 % of sulfate, 30% of secondary and 15% of primary organic aerosols, 14% of ammonium aerosols and less than 3% of black carbon. The analysis of the anthropogenic and biomass burning aerosols shows a positive trend for all aerosols simulated by CESM-MAM7.

1-Introduction

During boreal summer, major convective activity is driven by the Asian summer monsoon (ASM). The ASM-related convection combines both land convection over mainland Asia and maritime convection over surrounding seas. This dynamical mechanism acts as a pathway for the transport of trace gases and pollutants from the boundary layer to the UTLS (Upper Troposphere Lower Stratosphere) (Randel and Park, 2006; Park et al., 2007; Pan et al., 2016;

40   Gottschaldt et al., 2017). The upper atmospheric circulation is dominated by the related Asian
Monsoon Anticyclone (AMA), which is known to contain enhanced concentration of tropospheric
trace gases and aerosols, due to rapid lifting from the boundary layer by deep convection and
subsequent horizontal confinement. The AMA is confined by the subtropical westerly jet stream
in the north (~40–45°N) and the equatorial easterly jet stream in the south (~10–15°N), and

45   spans from 20–140 °E in the northern hemisphere. The altitude of maximum strength of the
anticyclonic circulation is around the local tropopause (17–18 km) (e.g., Dethof et al., 1999;
Bian et al., 2012; Ploeger et al., 2015; Garny and Randel, 2016; Pan et al., 2016, Brunamonti et
al., 2018). On a daily basis, the specific location, spatial extent and strength of the AMA depend
on the internal dynamical variability of the ASM (Randel and Park, 2006; Garny and Randel,

50   2013; Vogel et al., 2015; Pan et al., 2016). As suggested, the AMA can effectively trap
boundary layer pollutants and is associated with the formation of the Asian Tropopause Aerosol
Layer (ATAL) (Vernier et al., 2011, Vernier et al., 2013). The ATAL refers to an enhanced
aerosol layer near the tropopause over the Asian monsoon region extending from ~13 and 18
km altitudes. Its horizontal extension is determined by the AMA geometry, roughly in the broad

55   region bounded by approximately 5-105° E, 15-45° N (e.g. Vernier et al., 2015, Lau et al., 2018,
Bian et al., 2020). Combined satellite observations from SAGE (Stratospheric Aerosol and Gas
Experiment) II and CALIOP (Cloud-Aerosol LIDAR with Orthogonal Polarization) have highlighted
the presence of the ATAL since 1998, while it was not observed prior to that year (Vernier et al.,
2015). Model studies have suggested that the ATAL might have been present previously but

60   was masked by the overwhelming UTLS aerosols produced by the Mount Pinatubo eruption
(Neely et al., 2014).
The sources, chemical composition and spatial and temporal variability of the ATAL are not yet
well understood. Recent observations from the StratoClim (Stratospheric and upper
tropospheric processes for better climate predictions) aircraft campaign in 2017 and a few

65   recent balloon measurements from the BATAL (Balloon measurement campaigns of the Asian
Tropopause Aerosol Layer) 2015 campaign (Vernier et al., 2018), suggest that aerosol particles
in the ATAL may contain large amounts of sulfate, as well as organics, nitrates (including
ammonium nitrate), black carbon and dust (Vernier et al., 2015, 2018; Yu et al., 2017; Höpfner
et al., 2019). Different indications on the ATAL composition have been brought by a number of

70   modeling studies. Yu et al. (2015), using the CESM1 (Community Earth System Model) global
Earth system model coupled with the CARMA (Community Aerosol and Radiation Model for
Atmospheres) aerosol model, have suggested that the ATAL might be principally composed of
secondary organic and sulfate aerosols, as well as of primary organic aerosols. Using GEOS-
Chem (Goddard Earth Observing System with Chemistry) chemical transport model, Fairlie et al.

75   (2020) have found significant ammont of sulfate, ammonium, organic aerosol and nitrate in the
ATAL, with a predominat contribution of niitrate, as was identified previously by Gu et al. (2016)
using an earlier version of the model. Fadnavis et al. (2017) performed model simulations with
ECHAM6-HAM (European Centre Hamburg Model 6.3-Hamburg Aerosol Model) global aerosol-
climate model, and their simulations showed a persistent maximum of carbonaceous aerosols

80   in the ATAL region. Ma et al. (2019) using the ECHAM/MESSy (Modular Earth Submodel System)
for Atmospheric Chemistry (EMAC) general circulation model coupled with the Global Modal-

aerosol eXtension (GMXe) aerosol module have found that mineral dust and water-soluble compounds, like nitrate and sulfate, are the principal aerosols typology over the Tibetan Plateau, within the AMA. Therefore, existing modeling studies have proved to be able to

85 simulate the enhancement concentration of aerosols in the AMA region, even if a very large uncertainty in the composition of the ATAL remains.

A rising temporal trend of the ATAL optical signature in the AMA region has been observed (Vernier et al., 2015). The recent rising trends of sulfur dioxide and volatile organic compounds emissions in India are a candidate for explaining the appearance of the ATAL and its evolution.

90 This region have been proposed as the main source region of the ATAL (Vernier et al., 2015). Continental convective regions have also been shown to be the main contributors to the air trapped within the AMA with North India and South of the Tibetan Plateau as specific source areas (Tissier and Legras, 2016; Legras et al., 2019).

On the other hand, important contributions of natural sources, like dust, are expected. Xu et al.

95 (2015), using CALIOP and MISR (Multi-angle Imaging SpectroRadiometer) satellite data, have found that dust is one of the predominant aerosol over the Tibetan Plateau, and the same finding is reported by Ma et al. (2019), using the ECHAM model. Lau et al. (2018), driven by MERRA-2 data, have found abundant amounts of dust in the mid- and upper- troposphere over India and China during May to June due to the westerly transport from the Middle East desert,

100 during July-August these large quantities of dusts transported from the deserts are trapped and accumulated within the AMA and contributing to the ATAL formation.

It's also important to note that the ATAL formation and possible spatial and temporal variability is closely related to the dynamical variability of the AMA. Basha et al. (2019) have suggested that the spatial extent and strength of the AMA is greater during July and August compared to

105 June and September, and that the decadal variability is bigger at the edges of the anticyclone. As a consequence of the variability of atmospheric dynamics, some years show a stronger monsoon activity than others (Lau et al., 2018, Basha et al., 2019, Yuan et al., 2019) and this affects the ATAL formation, location and composition. Wei et al., (2019) have also found that the AMA exhibits intraseasonal variability between the Iranian Plateau and the Tibetan Plateau

110 with a quasy-biweekly oscillation.

This study provides further insight on the chemical composition of the ATAL and assesses its decadal variability composition and aerosols trends for the first time. To asses this, we have carried out long-term modeling of the ATAL using the Community Earth System Model (CESM 1.2) which embeds the Community Atmosphere Model (CAM5) coupled with the MAM7 (Modal

115 Aerosol Model) aerosol module. Our simulations cover an overall extended period of 16 years, from January 15th 2000 to December 15th 2015. Yuan et al., 2019 derived decadal trends for carbonaceous aerosols and dust in the ATAL using only meteorological reanalysis data, while in the present study a detailed chemistry and microphysic modelling is used to estimate trends for a larger aerosols composition.

120 The present paper is structured as follows. In Sect. 2, we describe the model and correlative data used for its validation. The validation is discussed in Sect.3. Results are presented and discussed in Sect. 4. Conclusions are drawn in Sect. 5.

2-Model set-up and satellite observations

2.1-The CESM-MAM7 model

125   Model simulations were performed using the global Community Earth System Model (CESM1.2), based on the Community Atmospheric Model (CAMS 5.1) with its full chemical core for both troposphere and stratosphere, coupled with the Modal Aerosol Model (MAM7). The MAM7 module treats the aerosol microphysics, size distribution and both internal and external mixing using seven modes. The seven modes are, specifically: Accumulation (a1), Aitken (a2), Primary

130   Carbon (a3), Fine Dust and Sea Salt (a5 and a4), and Coarse Dust and Sea Salt (a7 and a6) (Liu et. al 2012). Extraterrestrial aerosols are neglected in our model. Table 1 lists the aerosols and dry diameter size ranges of each mode. The size distributions of each mode are assumed to be log-normal.

Mode	Accumulation (a1)	Aitken (a2)	Primary Carbon (a3)	Fine Sea Salt (a4)	Fine Soil Dust (a5)	Coarse Sea Salt (a6)	Coarse Soil Dust (a7)
Aerosols species	Sulfate (SO_4) Ammonium (NH_4) Secondary Organic Aerosols (SOA) Primary Organic Aerosols (POM) Black Carbon (BC) Sea Salt	Sulfate (SO_4) Ammonium (NH_4) Secondary Organic Aerosols (SOA) Sea Salt	Primary Organic Aerosols (POM) Black Carbon (BC)	Seal Salt Sulfate (SO_4) Ammonium (NH_4)	Soil Dust Sulfate (SO_4) Ammonium (NH_4)	Seal Salt Sulfate (SO_4) Ammonium (NH_4)	Soil Dust Sulfate (SO_4) Ammonium (NH_4)
Size range (µm)	0.056–0.26	0.015–0.052	0.039–0.13	0.095–0.56	0.14–0.62	0.63–3.70	0.59–2.75

135   **Table 1: Predicted species for interstitial and cloud-borne components (see text) of each aerosol mode in MAM7 and dry diameter size ranges.**

   The total number of transported aerosol tracers by the 7 log-normal modes in MAM7 is 31. The transported precursor gas species are SO_2 (sulfur dioxide), H_2O_2 (hydrogen peroxide), DMS

140   (dimethyl sulfide), H_2SO_4 (sulfuric acid gas vapour), NH_3 (ammonia) and lumped semi-volatile organic species (Big Alkenes, Big Alkanes, Toluene, Isoprene and Monoterpenes).

   The MAM7 module explicitly treats the microphysics of sulfate (SO_4), ammonium (NH_4), sea-salt, dust, black carbon (BC), primary organic matter (POM), and secondary organic aerosol (SOA). It simulates nucleation, condensation, coagulation, dry deposition, wet removal, and water

145   uptake of aerosols. The formation of new particles by nucleation occurs in the Aiken mode, which is calculated using a ternary parameterization (H_2SO_4-NH_3-H_2O) and boundary nucleation (Merikanto et al., 2007). The inter- and intra-modal coagulation is calculated for Aitken, Accumulation and Primary Carbon modes.

150 In MAM7 the aerosol particles (AP) can exist in the "interstitial" state (AP that are suspended in clear or cloudy air) and "cloud-borne" state (AP attached to or contained within different hydrometeors, such as cloud droplets and/or ice crystals). The cloud-borne aerosols only include AP that are within stratiform (anvil) clouds, while the interstitial aerosols include both clear-sky AP and AP contained within convective clouds. This means that the AP in convective cloud droplets are lumped with the interstitial AP in the model and the interstitial aerosol

155 mixing ratios include the truly interstitial (i.e. "clear-sky/dry") AP and the "convective" cloud-borne AP.

As has been detailed in Wang et al. (2013), in CAM5-MAM7 cloud-borne aerosols in stratiform clouds are treated in a prognostic way in CAM5: their mixing ratios are saved between model

160 time steps and evolve as a result of source, sink, and transport processes. Their activation is parametrised using vertical velocity (resolved and sub-grid turbulent) and aerosol properties of all the modes, following Abdul-Razzak and Ghan (2000). The stratiform-cloud-borne AP are assumed to not interact with convective clouds. Cloud-borne aerosols in convective clouds are treated diagnostically: their mixing ratios are diagnosed each model time step (with no

165 "memory") from the interstitial aerosol mixing ratios. For a complete description of the CAM5-MAM7 model see Liu et al. (2012).

In our configuration, land, sea-ice, and rivers are interactive processes in CESM, whereas oceans are prescribed. The model horizontal grid resolution is 1.9°x2.5° in latitude x longitude and is has 56 vertical levels of altitude extending from the surface to approximately 45 km

170 altitude, with 30 levels in the troposphere and 10 levels in the UTLS, at a vertical resolution of approximately 1 km.

The following emissions are used in our simulations. Biogenic emissions for CO, isoprene, C_2H_4, C_2H_6, C_3H_6, C_3H_8, acetone, methanol and isoprene are taken from MEGAN-MACC emission inventory (Sindelarova et al., 2014). Anthropogenic emissions and biomass burning emissions

175 are based on the CMIP6 (Coupled Model Intercomparison Project Phase 6) inventories provided by the Community Emissions Data System (CEDS, http://www.globalchange.umd.edu/ceds/ceds-cmip6-data/). According to CEDS, the anthropogenic emissions are first scaled to EDGAR database for most emission species, then to national/regional inventories, e.g. REAS 2.1 (Regional Emission inventory in ASia version 2.1,

180 Kurokawa et al., 2013) in Asia, for SO_2, NOx, NMVOCs, CO and CH_4. For each inventory, scaling factors are calculated for years when inventory data are available. Where inventory data are not available over the specified scaling time frame, remaining scaling factors are interpolated and extended to provide a continuous trend (Hoesly et al., 2018). The biomass burning emissions for CMIP6 are based on merged satellite observation and fires models (van Marle et

185 al., 2017), using GFED4 (Global Fire Emissions Database version 4), which include small-magnitude fires (available from 1997 to 2015). The emission of sea salt aerosols from the ocean follows the parameterization of Märtensson et al. (2003), for aerosols with geometric diameter < 2.8 μm. For aerosols with a geometric diameter ≥ 2.8 μm, sea salt emissions follow the parameterization of Monahan et al. (1986). The emission of mineral dust particles is

190 calculated based on the Dust Entrainment and Deposition Model (Zender et al., 2003). Volcanic

SO₂ emissions were obtained through the Volcanic Emissions for Earth System Models (VolcanEESM) initiative, described by Mills et al. (2016). The VolcanEESM database contains estimates of total SO₂ emissions by volcanic eruptions over the 1850-2016 period.

The meteorology in the model has been nudged using MERRA2 (Modern-Era Retrospective analysis for Research and Applications, Version 2, https://rda.ucar.edu/datasets/ds313.3) data for the years 2000-2015.

We run our simulations for 16 years, from January 15th 2000 to December 15th 2015, using the CESM1.2 (CAM5) initial atmosphere state file at that date.

2.2-Correlative satellite data

Our simulations have been compared to satellite data from the Microwave Limb Sounder (MLS) and the Atmospheric Chemistry Experiment –Fourier Transform Spectrometer (ACE-FTS).

The MLS sounder was launched in July 2004 on-board the NASA Aura satellite. Measurements in the millimeter and submillimeter wavelength ranges are continuously made during both night and day every 165 km along the suborbital track, covering latitudes from 82° S to 82° N (Waters et al., 2006). Here, we use the MLS version 4.23 data set (Livesey et al., 2020) for CO (Pumphrey et al., 2007; Livesey et al., 2008) for selected years (2005 and 2008) and pressure levels in the UTLS. We use CO vertical profiles from 215 to 0.0046 hPa. For these pressure levels, the vertical resolution is about 5.1 km and the horizontal resolution about 570 km (at 147 hPa) (Livesey et al., 2020). The data precision is about 16 ppbv and the data accuracy is estimated at ±26 ppbv and ±30%.

The ACE-FTS instrument is an in infrared solar occultation spectrometer, providing profiles of the Earth since February 2004 from the Canadian satellite SCISAT-1 (Bernath et al., 2005). It operates in the wavelength range from 2.2 to 13.3 µm (750-4400 cm-1) with a spectral resolution of 0.02 cm-1. The data set provides 30 measurements per day for over 30 chemical species from 5 km (or cloud top) up to 150 km. The horizontal weighting function of a measurement has typically a width of ~300 km. The vertical resolution is < 4 km.

3-Model evaluation with satellite observations: CO distribution

We compare CO measurements from MLS and ACE-FTS with our simulations. While a direct comparison of aerosol extinction observations from various satellite instruments with CESM-MAM7 is not easy, e.g. due to the interference of clouds, using a trace gas (like CO) is a more straightforward approach for a comparison. In fact, three-dimensional summer distributions of CO show a distinct enhancement in the AMA and have been proved an ideal tracer to identify the AMA's location and to track the transport processes to the AMA (e.g. Park et al., 2008, Barret et al., 2016, Santee et al., 2017). The CO comparison enables an evaluation of the model's capacity to reproduce the large-scale dynamical and morphological features, which is related to the aerosol distribution.

Figures 1a and 1b show the average summer (June-July-August) CO distribution, for the year 2008, observed by MLS in the UTLS (Fig. 1a) and produced by CESM-MAM7 (Fig. 1b), at the pressure level of 147 hPa, for MLS, and 150 hPa (average between 160-140 hPa, 3 levels), for

230   CESM-MAM7. The locations of the general enhancement of CO mixing ratios in the AMA and of the absolute maximum above India are well reproduced by the model (i.e. they are consistent with MLS observations). This is encouraging towards the model's ability to reproduce the general transport and convection processes within and around the AMA. It should be noted that the pressure levels used in this comparison, for CESM-MAM7 and MLS, are not identical. In

235   addition, the vertical resolutions differ as well (about 5.1 km, for MLS, and about 1 km, for CESM-MAM7). Furthermore, the temporal samplings of satellite and model data also differ: for CESM-MAM7 the temporal sampling is twice a day (one simulation at noon and one at midnight), whereas MLS samples the Earth on distinct orbits, with a full global coverage every 3 days. Even though it is therefore possible that intensive short-time events are missed by

240   either CESM-MAM7 or MLS, the sampling bias is not expected to present a significant source of discrepancies for 3-month averages, as shown in Figures 1a and 1b.

Compared to MLS observations, the model underestimates the CO mixing ratio by about 30%. One possible reason for this underestimation could be an underestimation of biomass burning emissions in the model (obtained from GFED4), which are a significant source for CO. We have

245   also compared CESM-MAM7 HCN mixing ratios (a strong biomass burning tracer) with ACE-FTS HCN observations (comparison not shown here). This latter comparison shows a marked underestimation of modelled HCN amounts, which supports the hypothesis of an underestimation of biomass burning emissions. Stroppiana et al. (2010) have compared different biomass burning inventories for CO. For 2003, they found that the CO emissions range

250   from 365 Tg (GFED3) to 1422 Tg (VGT - Vegetation Emission Inventory (CNRS-LA)) (Tansey et al., 2008), with GFED at the low end of this variability. At difference of GFED3, GFED4 include upgrades like the inclusion of small fire burned areas, modified burned-area-to-burned-fraction conversion and a revised fuel consumption parameterization that causes global emissions to increase in comparison with the previous version (GFED3). However, the effects of these

255   adjustments vary spatially and in some regions like in the Southeast of Asia, North and South of Africa the CO biomass burning emissions are lower (see Van de Werf et al. 2017). This could explain the low bias in CO mixing ratios for our comparisons with satellite measurements.

While reproducing average (monthly) features is a probing test for our simulations, catching shorter-term processes and variability is even more challenging towards the description of a

260   complex phenomenon as the ATAL. Thus, we have also tested the model's ability to reproduce observed specific features in time frames of the order of a few days. Figure 1c shows an possible 'eddy shedding' case on July 4th to 6th 2005. During this short time period, a multi-centric AMA is observed by MLS, with rather multiple maxima in eastern Asia, instead of a classical individual maximum above the Himalayan region. Our CESM-MAM7 simulations

265   reasonably reproduce this pattern. They show a distributed pattern with maxima above eastern Asia, but also above western Asia (Fig. 1d), which is very consistent with MLS observations of Fig. 1c. For averages over only three days (rather than for the three months, as in the previous example), the sampling bias can play a significant role for the different patterns observed for MLS and CESM-MAM7. For CESM-MAM7 a smooth average is displayed over 3 days; for MLS,

270   however, more visible data points consist of not more than one measurement and thus generate a "patchier" distribution. Therefore, some short-term features might not have been

captured by the MLS instrument. Nevertheless, our simulations are very consistent with MLS observations for this short-term configuration.

275 We have also tested the vertical structures of CESM-MAM7 simulations, using an ACE-FTS CO mixing ratio profile in the UTLS (Fig. 1e). Observations with ACE-FTS have been chosen because of their better vertical resolution with respect to MLS. It has to be noted that the location and time of the ACE-FTS measurement profile and the model output are not exactly the same, but agree within 1° longitude, 4° latitude and within 2.5 h (see Figure 1e). The vertical distribution of CESM-MAM7 simulations shows a quite remarkable agreement with ACE-

280 FTS observations above 400 hPa. Up to the level of 400 hPa the model underestimates (as also shown for the previous examples with MLS, see Figure 1a-d) CO values by around 30%, with smaller underestimations between 400 and 200 hPa. For pressure levels lower than 180 hPa CESM-MAM7 and ACE-FTS show a remarkable consistency.

The comparison of simulated CO with observed MLS and ACE-FTS CO in the UTLS allows to

285 concluded that, except for a possible underestimation of CO emissions, the model is able to reproduce the position and spatial extend of the Asian monsoon anticyclone in our simulations.
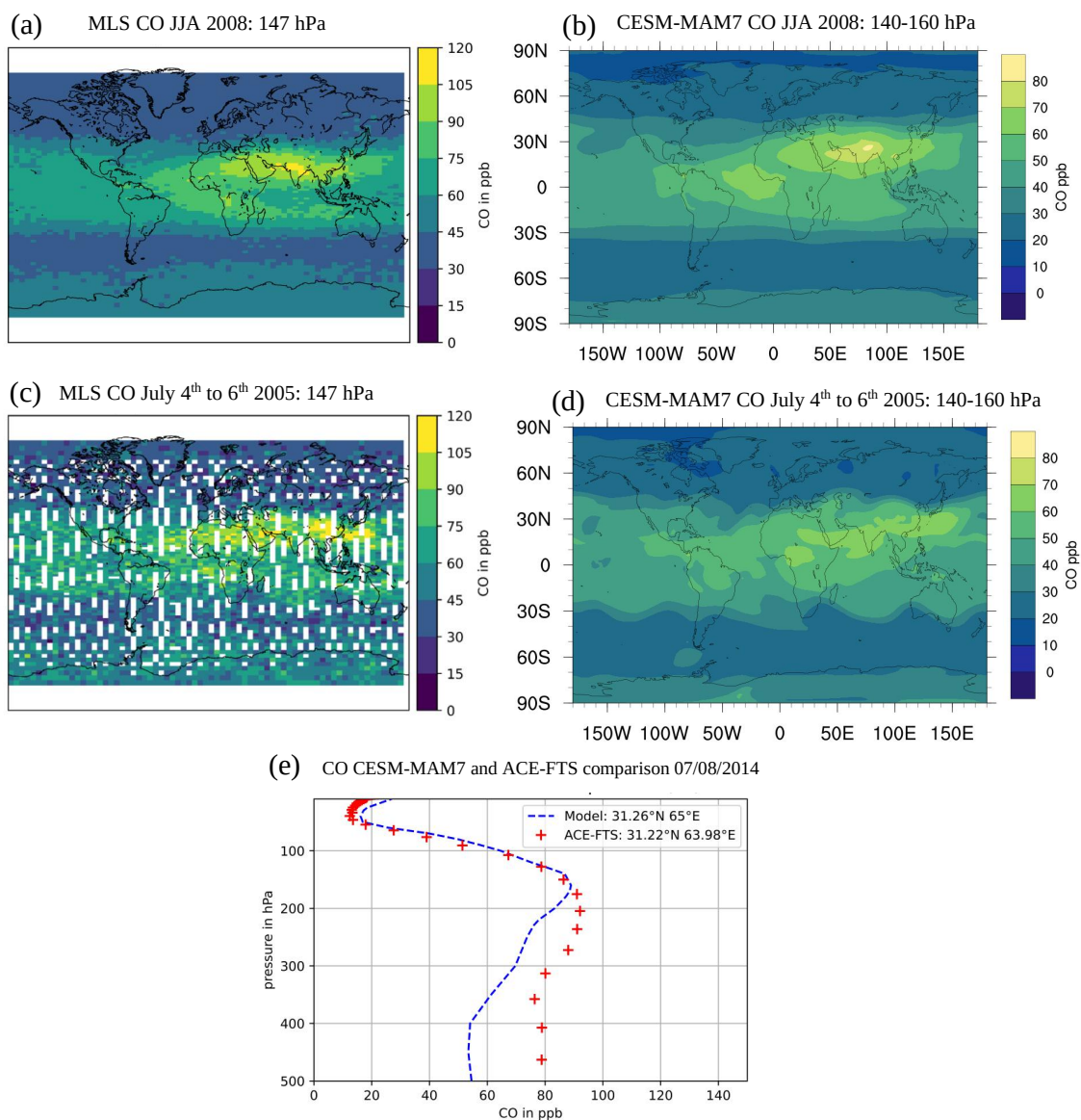
Figure 1: (a) Average MLS CO mixing ratio distribution for June-July-August 2008 at 147 hPa pressure level and (b) average CESM-MAM7 CO mixing ratio distribution for June-July-August 2008 between 140 and 160 hPa. (c) 3-day average for the MLS CO mixing ratios at 147 hPa (July 4th to 6th 2005) and (d) respective CESM-MAM7 simulations, for July 4th to 6th 2005 between 140 and 160 hPa. (e) ACE-FTS and CESM-MAM7 vertical CO profiles for Aug 7th 2014 at 31.22°N - 63.98°E, 14:30 UTC and 31.26°N, 65.00°E, 12:00 UTC, respectively.

## 4 - Results and Discussions

4.1 - Aerosol distribution and composition

Figure 2 shows the CESM-MAM7 regional distribution, over an extended area centered around
300 the AMA region, of different aerosol types: sulfate, SOA, POM, BC, ammonium and mineral dust.
The accumulation mode (a1) is here shown for all aerosol types, except for mineral dust (for
which Fine Soil Dust mode (a5) is shown). These maps represent average aerosol
concentrations, for July-August 2014, at three different pressure levels: 120, 100 and 80 hPa,
respectively (approximately 15.0, 16.5 and 18.0 km). Concentrations of sea salt particles, also
305 modelled in our study, are negligible and therefore are not shown in Fig. 2. The model
reproduces the horizontal distribution of the ATAL, i.e. an increase in aerosol concentration in
the AMA region with elevated aerosol concentration at 120-100 hPa (upper troposphere) and
noticeably decreasing for pressures lower than 80 hPa (altitudes higher than 18.0 km, lower
stratosphere).
310 Figure 2 shows that dust is the principal aerosol species in the ATAL, in terms of mass
concentration, in our simulations. These results agree with some previous modelling studies
(e.g. Fadnavis et al., 2013, Ma et al., 2019). According to Lau et al. (2018), high burdens of dust
are found in the ASM region, transported from the desert regions which are trapped by local
topography and accumulated to high concentration over the southern and eastern foothills of
315 the Tibetan Plateau and transported to the ATAL (~12-16 km) region by increased vertical
motion associated with deep convective motions. Other main aerosol components contributing
to the ATAL in our simulations, are sulfates, followed by SOA, POM, Ammonium and to a lesser
extent BC. Yu et al. (2015), using CESM1/CARMA model, have suggested that the ATAL (at
altitudes levels between 230-100 hPa) is principally composed of organics (~60 %) and sulfates
320 (~ 40%), while an aerosol enhancement due to dust above Africa is also obtained.
As discussed in previous studies, the spatial extent, strength and position of the AMA is highly
variable due to the dynamical seasonal variability of the ASM (Randel and Park, 2006; Garny
and Randel, 2013; Lau et al., 2018; Basha el al., 2019). Due to this dynamical variability the
tracer concentrations are strongly controlled by the oscillations and shedding of the AMA, that
325 therefore affect the ATAL extent and composition. For the subsequent analyses, we have
defined a criterion to isolate the ATAL horizontal extent based on the geopotential height (GPH)
values. For values of the GPH greater than 16.7 km, at 100 hPa, we tag the area as the AMA
region. Then, we use this criterion to choose a box with the highest probability to find air
masses delimited by the anticyclone. This criterion of empirically selected GPH values to
330 represent anticyclone boundaries has been discussed and used by several authors e.g.
Highwood and Hoskins (1998), Bergman et al. (2013), Barret et al. (2016), Pan et al. (2016).
Using this criterion, a wide region from around 20-130 °E and 20-45 °N is generally selected.
According to these considerations, we have chosen the box of 20-35 °N and 60-100 °E to
identify and study the ATAL composition (blue box in the central panel of first row in Fig. 2).

335
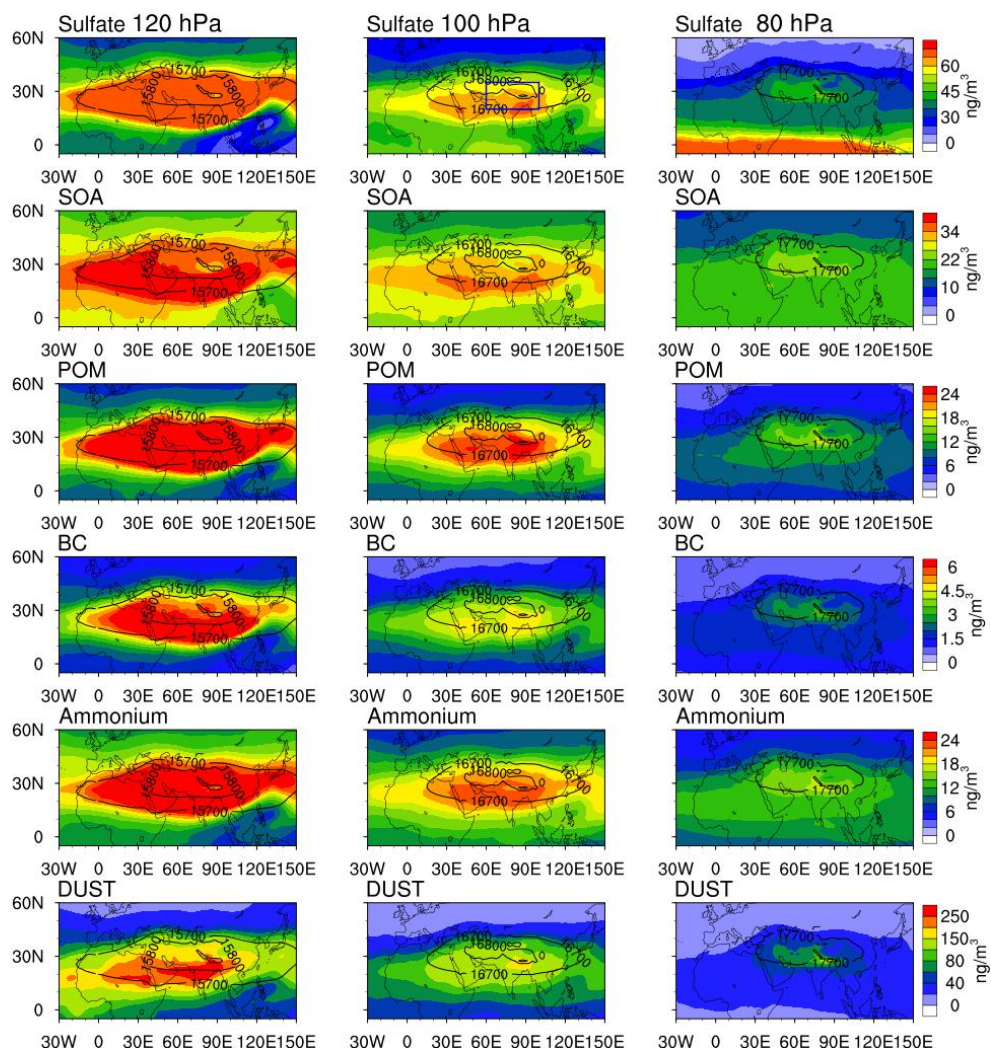
Figure 2: Spatial distribution of the aerosols mass concentration, averaged over July-August 2014, from CESM-MAM7 simulations, for six different aerosol types. From top to bottom row: sulfate, SOA, POM, BC, ammonium (in the accumulation mode) and mineral dust (in the fine dust soil mode). From left to right column: 120, 100 and 80 hPa pressure levels. Note the different color scale ranges. The black lines in the map represent the geopotential height > 15700 m at 120 hPa, >16700 m at 100 hPa and > 17700 m at 80 hPa. The blue box (2nd panel) represents the area chosen for the subsequent ATAL-specialised analyses (20-35 °N, 60-100 °E).

4.2 - Vertical distribution of the ATAL

In Fig. 3 we show CESM-MAM7 vertical aerosol mass mixing ratio profiles for the accumulation mode, averaged from June to August within the blue box of Fig. 2, for two selected years, 2000

and 2014. Our focus on the accumulation mode is justified by the fact that it is the principal mode that contributes to the ATAL (see Fig. S1 in Supplement), with mostly anthropogenic origin. In this first analysis, we have excluded dust. Dust is still the most important ATAL component, in our simulations, in terms of mass, but its burden and variability is mostly subject to natural factors and their variability.

A vertical region with marked localized increase of the concentration of all the aerosols types is observed, in particular between 300-80 hPa. This is what is expected as a manifestation of the ATAL, as it is broadly the vertical region where the AMA is located. The vertical structure of the AMA-related dynamics has been investigated by several authors (Bergman, J. et al., 2013; Garny and Randel, 2013; Brunamonti et al., 2018), showing evidence of deep convection and confinement extending up to 1.5–2.0 km above the cold-point tropopause. Enhanced aerosol backscatter also reveals the signature of the ATAL over the same altitude range (Vernier et al., 2015; Brunamonti et al., 2018). This location suggests that the existence of the layer is tied to a large-scale vertical transport in the anticyclone, i.e around 200 to 80 hPa (around 13 to 18 km) depending on the location and time.

Our simulations show a characteristic "double-peak" vertical configuration, with a bi-modal vertical distribution and two relative maxima, one at higher altitudes (~80-120 hPa) and the other at lower altitudes (~200-300 hPa). During early phases of the ASM (e.g., June, Fig. 3a) the maximum of aerosol concentrations is generally located between 200 and 80 hPa; later on (e.g., July and August, Figs. 3c,e) an aerosol enhancement at lower altitudes (around 250 hPa), superimposed with a maximum at around 100 hPa, is found. This "double-peak" vertical structure could be explained looking at the interplay of interstitial and in-clouds aerosols in CESM-MAM7. As was detailed in the Sect 2.1, the interstitial aerosols include both clear-sky/dry aerosols and aerosols contained within convective clouds. Our simulations show that that during the mature phase of the AMA (July and August), at the same time of increased convection, the AP in convective clouds (maximum of convective outflow at ~ 250 hPa) also increase. This causes a maximum of aerosols at lower altitudes. Figure S2 shows the cloud ice fraction for 2014 averaged for the blue box. In June the fraction of clouds is much smaller than in July and August.

We have also tried to separate the overall in-clouds and the purely dry aerosols (these latter likely coming from nucleation/condensation processes). In order to analyze the contribution of dry aerosols to the ATAL we have carried out an analysis to reduce/eliminate the contribution from convective cloud-borne aerosols. For this purpose, we have filtered out the profiles, in our blue box, for which the extinction coefficient is larger than an arbitrary threshold (1.0 10-3 km-1 in our case). Figure S3 shows the evaluation of different filters for the extinction coefficient applied for our box domain for August 2014 (same behavior is observed for July, not shown). We have applied a filter of 8.0 10-4, 9.0 10-4, 1.0 10-3 and 2.0x10-3 km-1, respectively and have evaluated the maximum value obtained at around 100 hPa. By varying these threshold values, we arrive to the point of isolating the upper peak, which is satisfactory for 1.0 10-3 km-1. Figures 3b,d,f show the vertical aerosols profiles with the applied filter, from where an isolated upper peak can be seen . This peak, due to the mentioned filtering, is associated with aerosols with limited extinctions. Large extinction values are associated with in-clouds aerosols,

which are larger in size due to liquid phase formation, freezing and/or hygroscopic growth (depending on the primary or secondary nature of aerosols). We then identify as clear sky/dry

395   AP the ones associated with this upper peak (120-80 hPa). The comparison with AP vertical profiles from Fig. 3a,c,e allows us to point out that in CESM-MAM7 both type of aerosols contribute to the ATAL, i.e. clear-sky/dry aerosols and convective cloud-borne aerosols.

It is worth noticing that, for these two selected years (2000 and 2014), the aerosol profiles can differ from one aerosol type to another, but are quite similar for a given month/year, and a

400   double peak/single peak structure can be observed for one aerosol type or another. This variability observed in the ATAL's vertical profiles also reflects the aspect of the dynamical variability of the AMA, which can be put in relationship with both the long-range transport and convection, as was shown in previous studies (e.g. Qie et al., 2014; Pan et al., 2016; Santee et al., 2017).
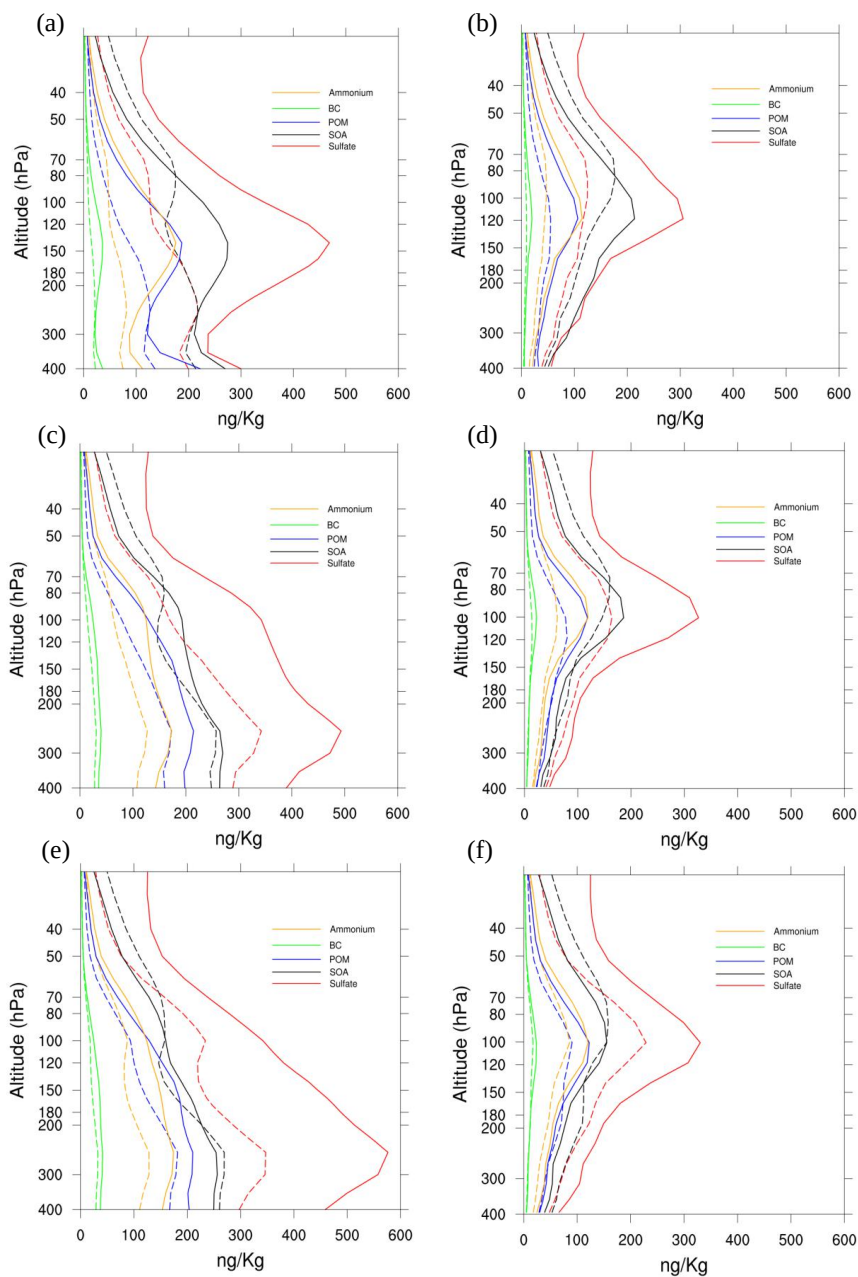
405

Figure 3: Vertical profiles of aerosol mass concentration of Sulfate, SOA, POM, Ammonium and BC in the accumulation mode (a1) in ng/kg averaged between 20-35 °N and 60-100 °E, the dash line correspond to the year 2000, solid lines the year 2014. (a) profile for June (c) July and (e) August. (b), (d), (f) same as (a), (c) and (e) but with the extinction filter applied.

410

Atmospheric
Chemistry
and Physics
Discussions

4.3 – Trends in aerosol composition of the ATAL

Figures 4a-d shows the annual average aerosol total mass concentrations for all the aerosol types simulated by CESM-MAM7, in the period 2000-2015, for all modes (Figs. 4a,c) and the

415 isolated accumulation mode (Fig. 4b,d). To account for the whole double-peak phenomenology and to isolate the single dry AP peak (see discussion in Sec. 4.2), the concentrations are averaged between 200-80 hPa (Fig. 4a,b) and 120-80 hPa (Fig. 4c,d). These two vertical ranges allow the differentiation of the ATAL composition based on in-clouds processes or, from another point of view, to describe how the composition changes depending on the altitude. No filter has

420 been applied to show the contribution of all aerosols.

The aerosol type that dominates the ATAL, for both altitude ranges, is dust, followed by sulfates and organic particles (secondary and primary). The comparison between Fig 4a and 4c shows that at higher altitudes the amount of sulfates increases slightly and, more markedly, dust amount decreases. Figure 4e shows the percent contribution of aerosols types to the ATAL,

425 between 120-80 hPa. It is evident that although less dust reaches higher altitudes, this aerosol type is still the mass-dominant aerosol type in the ATAL, contributing around 60%. This result agrees with previous studies. Ma et al. (2019) have shown that for the years 2010-2012 dust is one of the principal aerosol types over the Tibetan Plateau, reaching values > 100 ng/m^3. Our results show even larger amounts of dust, reaching values as large as about 200 ng/m^3. Lau et

430 al. (2018) using MERRA2 data have also reported large amounts of dust in the upper troposphere during the monsoon periods. Fadnavis et al. (2013) (also using a modal aerosol model (M7) in ECHAM5-HAMMOZ) have found that dominating aerosol types in the ATAL are dust and sulfates, followed by organic carbon and BC aerosols. The amount of sulfate, organic carbon and BC is quite similar to our results. However (see Figure 1 in Fadnavis et al., 2013),

435 the amount of dust reported is much smaller (around 30 ng/m^3 at 110 hPa) than our values. This discrepancy is probably due to the fact that: 1) they report averaged values from June to September and, 2) there are marked differences in the model online calculation for dust emission in ECHAM5 (e.g. wind speed, hydrological parameters and soil properties), with respect to our model. In the work of Yu et al. (2015), based on the CESM1/CARMA model, an

440 enhancement of concentration of aerosols above Africa, mainly attributed to dust, has been found. However, they do not report the amount of dust in the ATAL region. Even if there still is a large disagreement about the exact amount of dust present in the ATAL, it is clear that this natural component contributes significantly to the ATAL seasonal build-up due to its transport from the nearby desert regions, like Taklamakan and Thar deserts, and the northern slope

445 areas of Tibetan Plateau (Lau et al., 2018, Ma et al., 2019). The difference in the amount of dust reported by the different authors may be related to how the topography is represented in the model, the resolution of the model and the parameterization of the convection process (Brühl et al., 2018), as well as the different schemes used for the generation of dust.

With the intention to analyze the composition of the ATAL in terms of anthropogenic and

450 biomass burning emissions we discuss more in details the contribution of the non-dust aerosols, for which the accumulation mode at two different altitude ranges is shown in Fig. 4b, d. Excluding dust particles, the accumulation mode (a1, size range: 0.056-0.26 μm) is the

principal mode that contributes to the ATAL. This can be seen in the Fig. S1 in the Supplements.
Hence, anthropogenic and biomass burning aerosols that reach the ATAL are principally small
455   and young. The same behavior is observed in the 200-80 hPa range (Figure not shown here).
Sulfate aerosols from moderate-to-strong volcanic eruptions, with injection in the UTLS, can
also interact with the dynamical features of the AMA (e.g. Sellitto at al., 2017) and, under
certain conditions, can impact the ATAL aerosol population. Larger sulfate concentrations in
2009 and 2011 are linked to the volcanic eruptions of Sarychev (June 2009) and Nabro (June
460   2011). These eruptions injected large quantities of SO_2 into the UTLS, just before the onset of
the AMA. The subsequently formed volcanic sulfates from SO_2 conversion to particles rise the
background inside and outside the AMA and therefore contributed to the ATAL burden, during
these two years. For these years influenced by moderate volcanic eruptions the concentration
of sulfate increases drastically and reaches or even exceeds the dust concentration (see Fig. 4).
465   Excluding dust and focusing on the mostly anthropogenic accumulation mode, Fig. 4f suggest
that the fraction of the ATAL of anthropogenic origin is composed of about 40% Sulfate, 30%
SOA, 15% POM, 14% ammonium and less than 3% BC. Compared to the results reported by Yu
et al. (2015), our results show about the same percentage of sulfate in the ATAL but less
organics, i.e ~45% aggregating SOA and POM for our study compared with 60 % of organic as
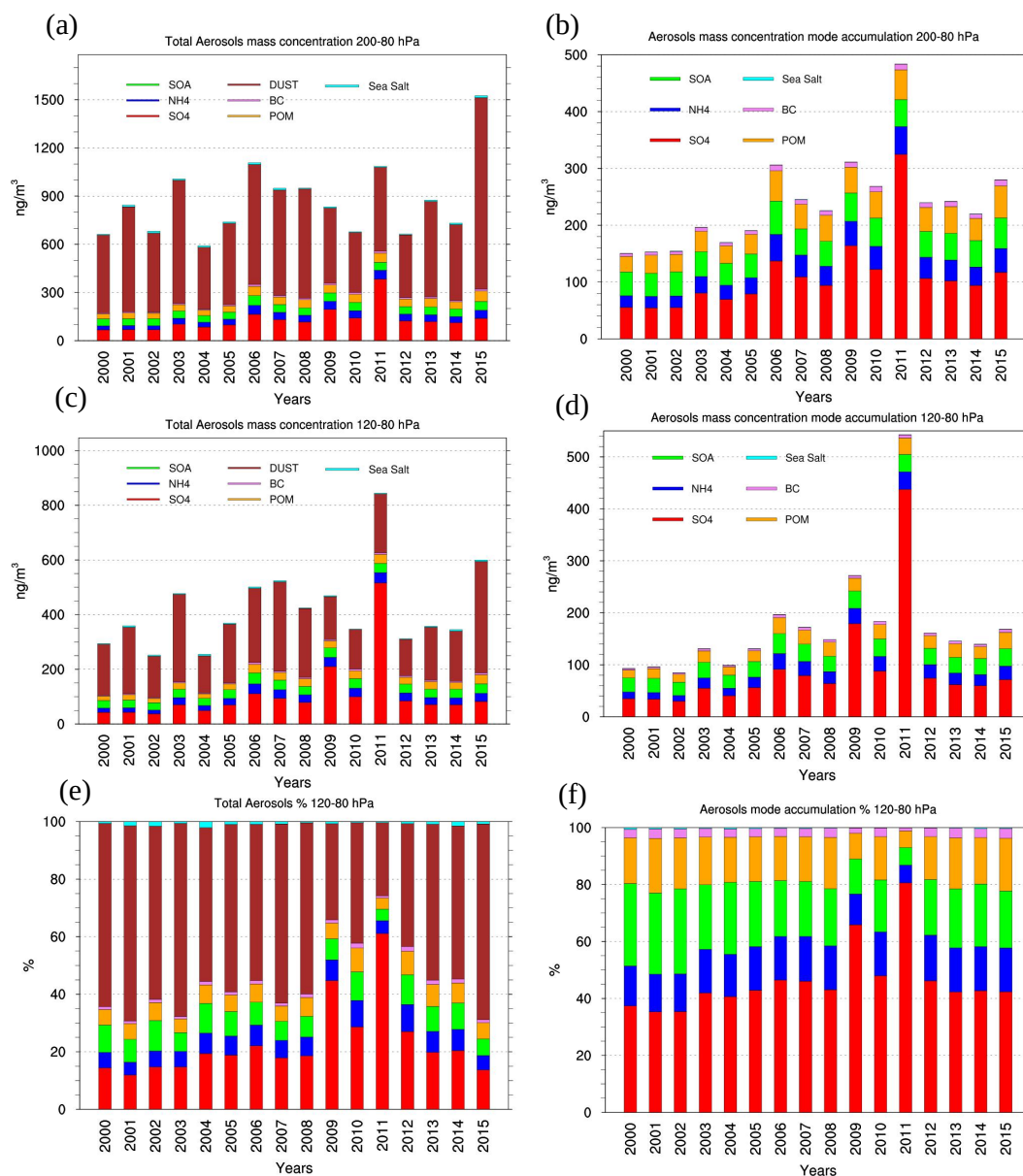470   reported by Yu et al. (2015).

Figure 4: Evolution of the total aerosol mass concentration of all the aerosol types present in CESM-MAM7 in all the modes averaged at 20-35°N, 60-100 °E for July-August, (a) between 200-80 hPa, (c) between 120-80 hPa , (e) percent amount at 120-80 hPa. Panels (b), (d) and (f) are the same as panels (a), (c) and (e) but only for the aerosols in the accumulation mode.

In the following, we evaluate the decadal trends of the different aerosol types in the ATAL. In particular, we have estimated the trends for the dust in the fine soil dust mode (Fig. 5a) and all other aerosol types in the accumulation mode (Figs. 5b,c). The concentrations for each year are averaged between 120-80 hPa pressure levels and over the domain chosen above (blue

17

Atmospheric
Chemistry
and Physics
Discussions

Open Access

EGU

box of Fig. 2), excluding the years with volcanic eruptions impacting the UTLS, i.e. 2005 to 2009 and 2011-2012 (Manam: April 2005; Soufrière Hills: August 2006; Tavurvur: October 2006; Okmok: August 2008; Kasatochi: August 2008; Sarychev: June 2009; Nabro: June 2011, taken from Khaykin et al. 2017, see Table 3 in their paper).

485 As can been see from Fig. 5a, dust does not display any clear trend and the p-value of 0.64 confirms an insignificant positive value (same behaviour is observed in the 200-80 hPa range, figure not showed here), reinforcing the evidence that the variation in dust concentration in the ATAL region is only subject to the natural interannual variability, as pointed out in Yuan et al. (2018), with no specific long-term trends. The sparse variations of dust in the ATAL reflects the

490 influence of other factors not related to the ASM, like the variability of extratropical westerlies that can strongly affect the long-range dust transport at high elevations, or the wet scavenging in and below clouds that can overcome the effect of lofting by deep convection. It has to be mentioned that dust modelling still suffers from several intrinsic limitations. The simulations of the dust cycle and its interactions with the Earth system depend on the empirical nature of

495 dust emission parameterizations in the models. The dust emissions are calculated online, and they are highly sensitive to the surface wind speed, i.e. to the meteorological data used. For example, Wu et al. (2018) have evaluated dust emissions in East Asia simulated by 15 climate models participating in the Coupled Model Intercomparison Project Phase 5 (CMIP5) during 1961-2005. They have found discrepancies with the observations for all the models, because

500 climate models may not sufficiently represent the trends of surface wind speeds and precipitation. This indicates that there is still a need to improve the representation of the dust cycle in climate models to simulate long-term dust changes.

Figures 5b,c show the trends for all the aerosols in the accumulation mode averaged in our box over the 120-80 hPa vertical level range, respectively without and with the extinction filter

505 applied so as to isolate dry from in-clouds (including from convective clouds) aerosols. All the aerosol types show an increase over the simulated 16-years. This mirrors the increase of the emissions in Asia. From Fig. 5b, it can be seen that sulfate aerosols trends in the ATAL, roughly doubling their concentration from ~36 ng/m^3 in 2000 to ~75 ng/m^3 in 2015 (i.e. about 108% increase in 15 years) an marked increases are also observed for POM (~80%), ammonium

510 (~100%) and BC (~93%), while for SOA the trend is weaker, i.e. going from ~ 27 to 33 ng/m^3 (~24%). The concentrations for the years 2000 and 2015, the increment, correlation and p-value are summarized in Tab. 2.

Figure 5c shows the trends of dry aerosols, i.e. with the extinction filter applied, in the ATAL between 120 and 80 hPa. The comparison between Fig. 5c with 5b, together with the values

515 reported in Tab. 2, show that the increasing trends and correlation values are slightly smaller than values reported without applying the filter. This reflects the fact that at 120-80 hPa the dry aerosols contribute to a larger fraction of the ATAL than convective cloud-borne aerosols.

The analysis of differences without and with the application of the extinction filter (i.e, (dry + convective) - (dry) aerosols) reveals that the increase for convective cloud-borne aerosols

520 between 120 and 80 hPa in our box domain is ~22% for sulfate, ~10% for SOA, ~28% for POM, ~ 20% for NH$_4$ and ~ 25% for BC (values derived from Tab. 2).

18

We have also carried out the same analysis for the larger altitude interval of the ATAL, i. e. between 200 and 80 hPa (Fig. 5d and e). More convective cloud-borne aerosols are likely in this case. Thus, the differences for the cases without versus with the extinction filter (calculated from Tab. 2) are larger than the previous case (~ 36% for sulfates, ~44% for POM, ~32% for NH$_4$, 47% for BC and ~ 21% for SOA).

Aerosol	SO$_4$	SOA	POM	NH$_4$	BC	DUST	SO$_4$	SOA	POM	NH$_4$	BC
120-80 hPa	Without Filter						Filter Extinction 1 x10^{-3} km^{-1}				
2000 (ng/m^3)	36	26.8	16.4	13.4	2.9	159	35.7	26.3	16	13.2	2.8
2015 (ng/m^3)	75	33.4	29.4	26.7	5.6	188	66.3	30	24.2	23.7	4.7
% increment	108.3	24.6	79.3	99.2	93.1	18.2	85.7	14	51.2	79.5	68
R coefficient	0.78	0.79	0.85	0.83	0.86	0.18	0.72	0.63	0.80	0.79	0.80
p-value	0.010	0.010	0.003	0.005	0.002	0.64	0.02	0.07	0.007	0.01	0.008
200-80 hPa	Without Filter						Filter Extinction 1 x10^{-3} km^{-1}				
2000 (ng/m^3)	53	37.7	26.5	19.6	4.7		39	27.6	18.3	14.4	3.2
2015 (ng/m^3)	108	47.5	46.3	37.9	9		65.2	28.8	23.9	23.2	4.6
% increment	103.8	26	75	93.4	91.5		67	4.3	30.6	61	44
R coefficient	0.87	0.84	0.88	0.88	0.89		0.70	0.27	0.74	0.74	0.74
p-value	0.002	0.003	0.001	0.001	0.0008		0.04	0.48	0.02	0.02	0.02

Table 2: Averaged aerosol mass concentration and percentage of the increase from 2000 to 2015 for SO$_4$, SOA, POM, NH$_4$ and BC, averaged for the summer period July-August at 20-35 °N, 60-100 °E between 120-80hPa and 200-80 hPa, without and with the extinction filter applied. R coefficient from Fig. 5b to 5e and the respective p-value are also reported.
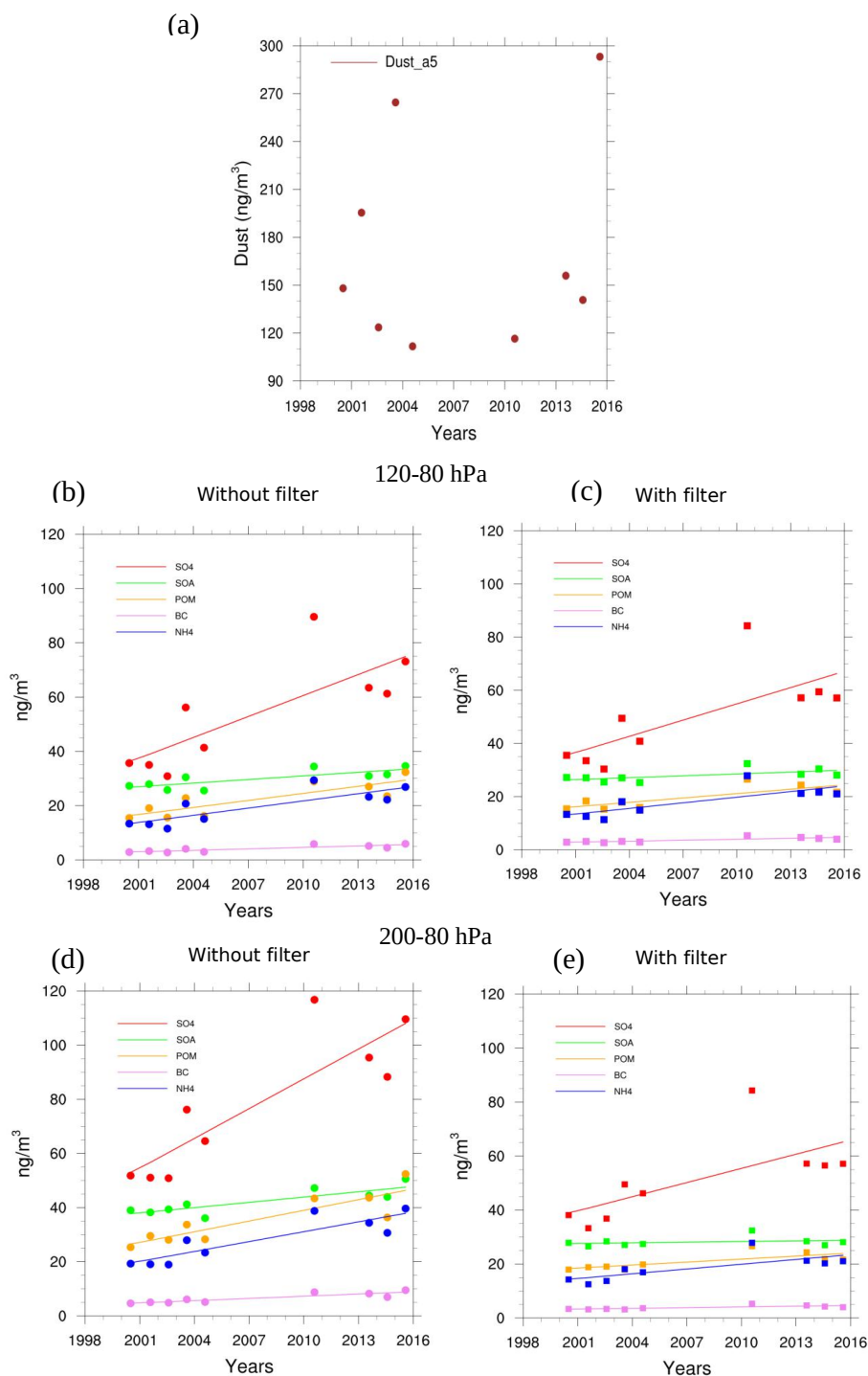
Figure 5: Aerosols mass concentration trends simulated by CESM-MAM7 averaged between 20-35 °N, 60-100°E for July and August. (a) for dust in the Fine Soil Dust mode between 120-80 hPa (b) respectively for SO₄, SOA, POM, BC, NH₄ in the accumulation mode between 120-

540   **80 hPa (c) Same as (b) but with the extinction filter applied. (d) and (e) same that (b) and (c) but averaged between 200-80 hPa. The plots show the trends excluding the years with volcanic eruptions impacting the UTLS.**

4.4 - Aerosol Optical Depth (AOD) of the ATAL

In Fig. 6 we show the aerosol optical depth (AOD) at 550 nm averaged for July-August and
545   between 20-35 °N latitude, for selected years between 2000 and 2015, as function of the longitude. As done before, two different altitude ranges, 200-80 hPa (Fig. 6a) and 120-80 hPa (Fig. 6b), are analyzed, to account for the double-peak ATAL introduced in Sect. 4.1. The AOD is calculated from the total aerosol extinction provided by CESM-MAM7. Then, in the AOD the extinction of all the aerosols from all modes and both dry aerosols and convective in-cloud
550   aerosols are taken into account in the AOD. For the full double-peak ATAL, AOD values from about 0.007, in 2000, to about 0.016, in 2015, are obtained in the core of the AMA region (Fig. 6a). These values are about a factor 2-3 larger than the values reported by Vernier et al. (2015), using SAGEII and CALIOP satellite data. The values reported by Vernier et al. (2015) include a cloud-screening procedure that might have screened out some of what we identify as the lower
555   peak from convective cloud-borne aerosols. It is important to mention that Vernier et al. (2015) have used hypotheses based on LiDAR observations and hypotheses on the LiDAR ratio value to derive the extinction coefficient to estimate the AOD. Yu et al. (2015), using the CESM1/CARMA model, have also reported an AOD with a factor of ~2 larger than Vernier et al. (2015). Our double-peak ATAL features highlighted in Fig. 6a are comparable with those of Yu
560   et al. (2015). However, the shape and maximum values in our plot (Fig. 6a) are slightly different from those of Yu et al. (2015), who have used a different latitudinal extent (15° to 45° N) to study the ATAL. Taking into account that dry aerosols dominate over the 120-80 hPa range, AOD values from about 0.0019, in 2000, to about 0.004, in 2015, are found for this vertical region (Fig. 6b). The difference between the AOD values obtained for the two altitude
565   ranges in Fig 6a and 6b points at the importance of what we have identified as convective in-cloud aerosols.

A net AOD increase of about a factor 2 is found from 2000 to 2015 both for the full double-peak ATAL and the dry ATAL-only aerosols, for the whole AMA region (0-120°E). However, for the first period (2000 to 2004) the increase of AOD is less pronounced, especially for latitudes
570   further east. The acceleration of the ATAL AOD increases and possible causes (increase in Asian emissions, more efficient vertical transport or other reasons) require further investigation and the continuous monitoring of ATAL burden and properties in the future.

(a) (b)
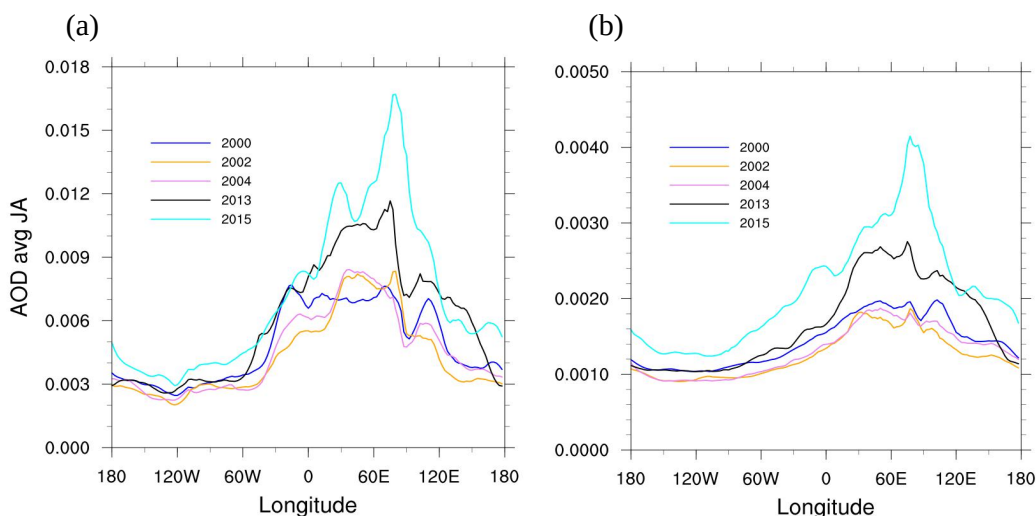
Figure 6: AOD at 550 nm averaged from 20-35 °N of latitude for July-August (a) between 200-80 hPa (around 13 to 18 km) (b) between 120-80 hPa (around 15.7 to 18 km). Different colors represent the different selected years.

5-Conclusions

In this paper, we have presented the results for our long-term simulation, i.e. 16 years (January 15th 2000- December 15th 2015), to investigate the composition and trends of the specific ATAL aerosols using the CESM-MAM7 model. The model was driven by the CMIP6 emissions inventory for the anthropogenic and biomass burning emissions of the principal trace gases and aerosols, while the biogenic emissions were taken from the MEGAN-MACC inventory. During summer, a confinement of polluted air masses has been found within the AMA region, which is tied to the ATAL position. The model evaluation with MLS and ACE-FTS satellite data reflects that transport and convection features are well represented in our simulations, despite a possible underestimation of the biomass burning emissions.

The results show that dust is the dominating aerosol type in terms of mass in the ATAL in agreement with other studies (e.g. Ma et al., 2019). Our modeled burdens of dust in the ATAL are larger than what has been reported in the past. The parameterizations of dust emissions are sensitive to the topography representation, the resolution and the parameterizations of the convection processes used in the model, which can partially explain these differences. These results suggest the need for further improvements of the representation of dust-affected fields in climate models. Apart from dust, the average partitioning for other aerosol types contained in the ATAL (from anthropogenic and from biomass burning emissions) is the following: 40% Sulfate, 30% Secondary Organic Aerosols, 15% Primary Organic Matter, 14% Ammonium and less than 3% Black Carbon. Nitrate aerosols are expected to be an important aerosol component in Asia (e.g. Höpfner et al., 2019) due to the increase of nitrogen-oxides and

Atmospheric
Chemistry
and Physics
Discussions

ammonia emissions, but is not simulated in our work because their treatment in MAM7 is

600 computationally expensive.

For non-dust aerosols the accumulation mode dominates anthropogenic/biomass burning ATAL's aerosols, a marked positive trend of anthropogenic and biomass burning aerosol concentrations is found, with up to a factor two increase of mass concentrations between 2000 and 2015. On the contrary, mineral dust does not show a clear positive trend, probably due to

605 the fact that dust burdens are mainly driven by natural variability.

In terms of vertical distributions, our simulations reveal a marked double-peak structure. The CESM-MAM7 simulations have allowed as to analyze separately 'clear sky/dry' aerosols and 'cloud-borne' aerosols, including those from convective clouds. Dry aerosols contribute to one higher peak (peaking around 80-120 hPa) and convective cloud-borne aerosol to one lower

610 peak (peaking around 200-250 hPa). We show that the contribution of the convective cloud-borne aerosols to the ATAL generally increases during the phases of mature and late ATAL, in July-August, shifting the maximum of aerosols concentrations to lower altitudes. The dry aerosols are generally dominating in the early phases of ATAL.

The obtained AOD values show an enhancement by a factor ~2 between the 200-80 hPa and

615 120-80 hPa levels. Relatively large AOD values are observed for the 200-80 hPa layer increasing from 0.007 in 2000 to 0.016 in 2015. These large values mirror the fact that extinction coefficients take into account the complete double-peak ATAL, including both dry and convective cloud-borne aerosols.

635 *Data availability*

MERRA-2 reanalysis data are available at http://rda.ucar.edu/datasets/ds313.3/

CMIP6 emissions files are available at https://svn-ccsm-inputdata.cgd.ucar.edu/trunk/inputdata/atm/cam/chem/emis/CMIP6_emissions_1750_2015/

ACE-FTS https://database.scisat.ca/level2/

640   MLS data https://mls.jpl.nasa.gov/data/

Code availability

The release version 1.2.2 of CESM can be download from http://www.cesm.ucar.edu/models/cesm1.2/tags/index.html#CESM1_2_2

645

Author Contribution

AB, PS, GB and FJ designed the research and the analyse and interpretation of the model results. AB performed the model simulation with the support from FJ. CK performed the satellite analysis from MLS and ACE-FTS data. BL was involved in the discussion and results
650   interpretation. AB prepared the manuscript with the contribution and discussions from all the co-authors.

References

Abdul-Razzak, H. and Ghan, S. J.: A parameterization of aerosol activation: 2. Multiple aerosol
655   types, J. Geophys. Res. Atmos., 105(D5), 6837–6844, doi:10.1029/1999JD901161, 2000.
Adams, P. J. and Seinfeld, J. H.: Predicting global aerosol size distributions in general circulation models, J. Geophys. Res. Atmos., 107(D19), AAC 4-1-AAC 4-23, doi:10.1029/2001JD001010, 2002.

660   Barret, B., Sauvage, B., Bennouna, Y. and Le Flochmoen, E.: Upper-tropospheric CO and O3 budget during the Asian summer monsoon, Atmos. Chem. Phys., 16(14), 9129–9147, doi:10.5194/acp-16-9129-2016, 2016.

Basha, G., Ratnam, M. V and Kishore, P.: Asian Summer Monsoon Anticyclone: Trends and
665   Variability, Atmos. Chem. Phys. Discuss., 2019, 1–30, doi:10.5194/acp-2019-668, 2019.
Bergman, J. W., Fierli, F., Jensen, E. J., Honomichl, S. and Pan, L. L.: Boundary layer sources for the Asian anticyclone: Regional contributions to a vertical conduit, J. Geophys. Res. Atmos., 118(6), 2560–2575, doi:10.1002/jgrd.50142, 2013.

670   Bernath, P. F., McElroy, C. T., Abrams, M. C., Boone, C. D., Butler, M., Camy-Peyret, C., Carleer, M., Clerbaux, C., Coheur, P.-F., Colin, R., DeCola, P., DeMazière, M., Drummond, J. R., Dufour, D., Evans, W. F. J., Fast, H., Fussen, D., Gilbert, K., Jennings, D. E., Llewellyn, E. J., Lowe, R. P., Mahieu, E., McConnell, J. C., McHugh, M., McLeod, S. D., Michaud, R., Midwinter, C., Nassar, R., Nichitiu, F., Nowlan, C., Rinsland, C. P., Rochon, Y. J., Rowlands, N., Semeniuk, K., Simon, P.,
675   Skelton, R., Sloan, J. J., Soucy, M.-A., Strong, K., Tremblay, P., Turnbull, D., Walker, K. A., Walkty, I., Wardle, D. A., Wehrle, V., Zander, R. and Zou, J.: Atmospheric Chemistry Experiment (ACE): Mission overview, Geophys. Res. Lett., 32(15), doi:10.1029/2005GL022386, 2005.

Bian, J., Pan, L. L., Paulik, L., Vömel, H., Chen, H. and Lu, D.: In situ water vapor and ozone
680   measurements in Lhasa and Kunming during the Asian summer monsoon, Geophys. Res. Lett.,
39(19), doi:10.1029/2012GL052996, 2012.

Bian, J., Li, D., Bai, Z., Li, Q., Lyu, D. and Zhou, X.: Transport of Asian surface pollutants to the
global stratosphere from the Tibetan Plateau region during the Asian summer monsoon, Natl.
685   Sci. Rev., 7(3), 516–533, doi:10.1093/nsr/nwaa005, 2020.

Binkowski, F. S. and Roselle, S. J.: Models-3 Community Multiscale Air Quality (CMAQ) model
aerosol   component   1.   Model   description,   J.   Geophys.   Res.   Atmos.,   108(D6),
doi:10.1029/2001JD001409, 2003.

690

Brunamonti, S., Jorge, T., Oelsner, P., Hanumanthu, S., Singh, B. B., Kumar, K. R., Sonbawne, S.,
Meier, S., Singh, D., Wienhold, F. G., Luo, B. P., Boettcher, M., Poltera, Y., Jauhiainen, H.,
Kayastha, R., Karmacharya, J., Dirksen, R., Naja, M., Rex, M., Fadnavis, S. and Peter, T.: Balloon-
borne measurements of temperature, water vapor, ozone and aerosol backscatter on the
695   southern slopes of the Himalayas during StratoClim 2016-2017, Atmos. Chem. Phys., 18(21),
15937–15957, doi:10.5194/acp-18-15937-2018, 2018.

Brühl, C., Schallock, J., Klingmüller, K., Robert, C., Bingen, C., Clarisse, L., Heckel, A., North, P.
and Rieger, L.: Stratospheric aerosol radiative forcing simulated by the chemistry climate
700   model EMAC using Aerosol CCI satellite data, Atmos. Chem. Phys., 18(17), 12845–12857,
doi:10.5194/acp-18-12845-2018, 2018.

Dethof, A., O'Neill, A., Slingo, J. M. and Smit, H. G. J.: A mechanism for moistening the lower
stratosphere involving the Asian summer monsoon, Q. J. R. Meteorol. Soc., 125(556), 1079–
705   1106, doi:10.1002/qj.1999.49712555602, 1999.

Fadnavis, S., Semeniuk, K., Pozzoli, L., Schultz, M. G., Ghude, S. D., Das, S. and Kakatkar, R.:
Transport of aerosols into the UTLS and their impact on the Asian monsoon region as seen in a
global model simulation, Atmos. Chem. Phys., 13(17), 8771–8786, doi:10.5194/acp-13-8771-
710   2013, 2013.

Fadnavis, S., Kalita, G., Kumar, K. R., Gasparini, B. and Li, J.-L. F.: Potential impact of
carbonaceous aerosol on the upper troposphere and lower stratosphere (UTLS) and
precipitation during Asian summer monsoon in a global model simulation, Atmos. Chem. Phys.,
715   17(18), 11637–11654, doi:10.5194/acp-17-11637-2017, 2017.

Fairlie, T. D., Liu, H., Vernier, J.-P., Campuzano-Jost, P., Jimenez, J. L., Jo, D. S., Zhang, B.,
Natarajan, M., Avery, M. A. and Huey, G.: Estimates of Regional Source Contributions to the
Asian Tropopause Aerosol Layer Using a Chemical Transport Model, J. Geophys. Res. Atmos.,
720   125(4), e2019JD031506, doi:10.1029/2019JD031506, 2020.

Garny, H. and Randel, W. J.: Dynamic variability of the Asian monsoon anticyclone observed in potential vorticity and correlations with tracer distributions, J. Geophys. Res. Atmos., 118(24), 13,413-421,433, doi:10.1002/2013JD020908, 2013.

725 Garny, H. and Randel, W. J.: Transport pathways from the Asian monsoon anticyclone to the stratosphere, Atmos. Chem. Phys., 16(4), 2703–2718, doi:10.5194/acp-16-2703-2016, 2016.

Gelaro, R., McCarty, W., Suárez, M. J., Todling, R., Molod, A., Takacs, L., Randles, C. A., Darmenov, A., Bosilovich, M. G., Reichle, R., Wargan, K., Coy, L., Cullather, R., Draper, C., Akella, S., Buchard, V., Conaty, A., da Silva, A. M., Gu, W., Kim, G.-K., Koster, R., Lucchesi, R., Merkova,

730 D., Nielsen, J. E., Partyka, G., Pawson, S., Putman, W., Rienecker, M., Schubert, S. D., Sienkiewicz, M. and Zhao, B.: The Modern-Era Retrospective Analysis for Research and Applications, Version 2 (MERRA-2), J. Clim., 30(14), 5419–5454, doi:10.1175/JCLI-D-16-0758.1, 2017.

735 Gottschaldt, K.-D., Schlager, H., Baumann, R., Bozem, H., Eyring, V., Hoor, P., Jöckel, P., Jurkat, T., Voigt, C., Zahn, A. and Ziereis, H.: Trace gas composition in the Asian summer monsoon anticyclone: a case study based on aircraft observations and model simulations, Atmos. Chem. Phys., 17(9), 6091–6111, doi:10.5194/acp-17-6091-2017, 2017.

740 Gu, Y., Liao, H. and Bian, J.: Summertime nitrate aerosol in the upper troposphere and lower stratosphere over the Tibetan Plateau and the South Asian summer monsoon region, Atmos. Chem. Phys., 16(11), 6641–6663, doi:10.5194/acp-16-6641-2016, 2016.

Highwood, E. J. and Hoskins, B. J.: The tropical tropopause, Q. J. R. Meteorol. Soc., 124(549), 1579–1604, doi:10.1002/qj.49712454911, 1998.

745

Hoesly, R. M., Smith, S. J., Feng, L., Klimont, Z., Janssens-Maenhout, G., Pitkanen, T., Seibert, J. J., Vu, L., Andres, R. J., Bolt, R. M., Bond, T. C., Dawidowski, L., Kholod, N., Kurokawa, J.-I., Li, M., Liu, L., Lu, Z., Moura, M. C. P., O'Rourke, P. R. and Zhang, Q.: Historical (1750-2014) anthropogenic emissions of reactive gases and aerosols from the Community Emissions Data

750 System (CEDS), Geosci. Model Dev., 11(1), 369–408, doi:10.5194/gmd-11-369-2018, 2018.

Höpfner, M., Ungermann, J., Borrmann, S., Wagner, R., Spang, R., Riese, M., Stiller, G., Appel, O., Batenburg, A. M., Bucci, S., Cairo, F., Dragoneas, A., Friedl-Vallon, F., Hünig, A., Johansson, S., Krasauskas, L., Legras, B., Leisner, T., Mahnke, C., Möhler, O., Molleker, S., Müller, R., Neubert,

755 T., Orphal, J., Preusse, P., Rex, M., Saathoff, H., Stroh, F., Weigel, R. and Wohltmann, I.: Ammonium nitrate particles formed in upper troposphere from ground ammonia sources during Asian monsoons, Nat. Geosci., 12(8), 608–612, doi:10.1038/s41561-019-0385-8, 2019.

Huang, J., Minnis, P., Yi, Y., Tang, Q., Wang, X., Hu, Y., Liu, Z., Ayers, K., Trepte, C. and Winker,

760 D.: Summer dust aerosols detected from CALIPSO over the Tibetan Plateau, Geophys. Res. Lett., 34(18), doi:10.1029/2007GL029938, 2007.

Khaykin, S. M., Godin-Beekmann, S., Keckhut, P., Hauchecorne, A., Jumelet, J., Vernier, J.-P., Bourassa, A., Degenstein, D. A., Rieger, L. A., Bingen, C., Vanhellemont, F., Robert, C., DeLand, M. and Bhartia, P. K.: Variability and evolution of the midlatitude stratospheric aerosol budget from 22 years of ground-based lidar and satellite observations, Atmos. Chem. Phys., 17(3), 1829–1845, doi:10.5194/acp-17-1829-2017, 2017.

Kloss, C., Berthet, G., Sellitto, P., Ploeger, F., Bucci, S., Khaykin, S., Jégou, F., Taha, G., Thomason, L. W., Barret, B., Le Flochmoen, E., von Hobe, M., Bossolasco, A., Bègue, N. and Legras, B.: Transport of the 2017 Canadian wildfire plume to the tropics via the Asian monsoon circulation, Atmos. Chem. Phys., 19(21), 13547–13567, doi:10.5194/acp-19-13547-2019, 2019.
Kurokawa, J., Ohara, T., Morikawa, T., Hanayama, S., Janssens-Maenhout, G., Fukui, T., Kawashima, K. and Akimoto, H.: Emissions of air pollutants and greenhouse gases over Asian regions during 2000–2008: Regional Emission inventory in ASia (REAS) version 2, Atmos. Chem. Phys., 13(21), 11019–11058, doi:10.5194/acp-13-11019-2013, 2013.

Lau, W. K. M., Yuan, C., Li, Z. and Li, Z.: Origin, Maintenance and Variability of the Asian Tropopause Aerosol Layer (ATAL): The Roles of Monsoon Dynamics, Sci. Rep., 8(1), 2045–2322, doi:10.1038/s41598-018-22267-z, 2018.

Legras, B. and Bucci, S.: Confinement of air in the Asian monsoon anticyclone and pathways of convective air to the stratosphere during summer season, Atmos. Chem. Phys. Discuss., 2019, 1–37, doi:10.5194/acp-2019-1075, 2019.

Li, Q., Jiang, J. H., Wu, D. L., Read, W. G., Livesey, N. J., Waters, J. W., Zhang, Y., Wang, B., Filipiak, M. J., Davis, C. P., Turquety, S., Wu, S., Park, R. J., Yantosca, R. M. and Jacob, D. J.: Convective outflow of South Asian pollution: A global CTM simulation compared with EOS MLS observations, Geophys. Res. Lett., 32(14), doi:10.1029/2005GL022762, 2005.

Liousse, C., Guillaume, B., Grégoire, J. M., Mallet, M., Galy, C., Pont, V., Akpo, A., Bedou, M., Castéra, P., Dungall, L., Gardrat, E., Granier, C., Konaré, A., Malavelle, F., Mariscal, A., Mieville, A., Rosset, R., Serça, D., Solmon, F., Tummon, F., Assamoi, E., Yboué, V. and Van Velthoven, P.: Updated African biomass burning emission inventories in the framework of the AMMA-IDAF program, with an evaluation of combustion aerosols, Atmos. Chem. Phys., 10(19), 9631–9646, doi:10.5194/acp-10-9631-2010, 2010.

Liu, X., Easter, R. C., Ghan, S. J., Zaveri, R., Rasch, P., Shi, X., Lamarque, J.-F., Gettelman, A., Morrison, H., Vitt, F., Conley, A., Park, S., Neale, R., Hannay, C., Ekman, A. M. L., Hess, P., Mahowald, N., Collins, W., Iacono, M. J., Bretherton, C. S., Flanner, M. G. and Mitchell, D.: Toward a minimal representation of aerosols in climate models: description and evaluation in the Community Atmosphere Model CAM5, Geosci. Model Dev., 5(3), 709–739, doi:10.5194/gmd-5-709-2012, 2012.

805 Livesey, N. J., Filipiak, M. J., Froidevaux, L., Read, W. G., Lambert, A., Santee, M. L., Jiang, J. H., Pumphrey, H. C., Waters, J. W., Cofield, R. E., Cuddy, D. T., Daffer, W. H., Drouin, B. J., Fuller, R. A., Jarnot, R. F., Jiang, Y. B., Knosp, B. W., Li, Q. B., Perun, V. S., Schwartz, M. J., Snyder, W. V, Stek, P. C., Thurstans, R. P., Wagner, P. A., Avery, M., Browell, E. V, Cammas, J.-P., Christensen, L. E., Diskin, G. S., Gao, R.-S., Jost, H.-J., Loewenstein, M., Lopez, J. D., Nedelec, P., Osterman, G.

810 B., Sachse, G. W. and Webster, C. R.: Validation of Aura Microwave Limb Sounder O3 and CO observations in the upper troposphere and lower stratosphere, J. Geophys. Res. Atmos., 113(D15), doi:10.1029/2007JD008805, 2008.

Livesey, N. J., Read, W. G., Wagner, P. A., Froidevaux, L., Lambert, A., Manney, G. L., Millán

815 Valle, L. F., Pumphrey, H. C., Santee, M. L., Schwartz, M. J., Wang, S., Fuller, R. A., Jarnot, R. F., Knosp, B. W., Martinez, E., and Lay, R. R.: Version 4.2x Level 2 and 3 data quality and description document, Jet Propul. Lab., Tech. Rep. JPL D-33509 Rev. E, Pasadena, CA, USA, availableat: http://mls.jpl.nasa.gov (20 April 2020), 2020.

820 Ma, J., Brühl, C., He, Q., Steil, B., Karydis, V. A., Klingmüller, K., Tost, H., Chen, B., Jin, Y., Liu, N., Xu, X., Yan, P., Zhou, X., Abdelrahman, K., Pozzer, A. and Lelieveld, J.: Modeling the aerosol chemical composition of the tropopause over the Tibetan Plateau during the Asian summer monsoon, Atmos. Chem. Phys., 19(17), 11587–11612, doi:10.5194/acp-19-11587-2019, 2019.
Mårtensson, E. M., Nilsson, E. D., de Leeuw, G., Cohen, L. H. and Hansson, H.-C.: Laboratory

825 simulations and parameterization of the primary marine aerosol production, J. Geophys. Res. Atmos., 108(D9), doi:10.1029/2002JD002263, 2003.

Merikanto, J., Napari, I., Vehkamäki, H., Anttila, T. and Kulmala, M.: New parameterization of sulfuric acid-ammonia-water ternary nucleation rates at tropospheric conditions, J. Geophys.

830 Res. Atmos., 12(D15), doi:10.1029/2006JD007977, 2007.

Mills, M. J., Schmidt, A., Easter, R., Solomon, S., Kinnison, D. E., Ghan, S. J., Neely III, R. R., Marsh, D. R., Conley, A., Bardeen, C. G. and Gettelman, A.: Global volcanic aerosol properties derived from emissions, 1990–2014, using CESM1(WACCM), J. Geophys. Res. Atmos., 121(5),

835 2332–2348, doi:10.1002/2015JD024290, 2016.

Monahan, E. C., Spiel, D. E. and Davidson, K. L.: A Model of Marine Aerosol Generation Via Whitecaps and Wave Disruption, in Oceanographic Sciences Library, pp. 167–174, Springer Netherlands., 1986.

840

Neely, R., Yu, P., Rosenlof, K., B. Toon, O., S. Daniel, J., Solomon, S. and L. Miller, H.: The contribution of anthropogenic SO2 emissions to the Asian tropopause aerosol layer, J. Geophys. Res, 119, doi:10.1002/2013JD020578, 2014.

845 Pan, L. L., Honomichl, S. B., Kinnison, D. E., Abalos, M., Randel, W. J., Bergman, J. W. and Bian, J.: Transport of chemical tracers from the boundary layer to stratosphere associated with the

Atmospheric
Chemistry
and Physics
Discussions

dynamics of the Asian summer monsoon, J. Geophys. Res., 121(23), 14,114-159,174, doi:10.1002/2016JD025616, 2016.

850 Park, M., Randel, W. J., Gettelman, A., Massie, S. T. and Jiang, J. H.: Transport above the Asian summer monsoon anticyclone inferred from Aura Microwave Limb Sounder tracers, J. Geophys. Res. Atmos., 112(D16), doi:10.1029/2006JD008294, 2007.

Park, M., Randel, W. J., Emmons, L. K., Bernath, P. F., Walker, K. A. and Boone, C. D.: Chemical
855 isolation in the Asian monsoon anticyclone observed in Atmospheric Chemistry Experiment (ACE-FTS) data, Atmos. Chem. Phys., 8(3), 757–764, doi:10.5194/acp-8-757-2008, 2008.

Ploeger, F., Gottschling, C., Griessbach, S., Grooß, J.-U., Guenther, G., Konopka, P., Müller, R., Riese, M., Stroh, F., Tao, M., Ungermann, J., Vogel, B. and von Hobe, M.: A potential vorticity-
860 based determination of the transport barrier in the Asian summer monsoon anticyclone, Atmos. Chem. Phys., 15(22), 13145–13159, doi:10.5194/acp-15-13145-2015, 2015.

Pumphrey, H. C., Filipiak, M. J., Livesey, N. J., Schwartz, M. J., Boone, C., Walker, K. A., Bernath, P., Ricaud, P., Barret, B., Clerbaux, C., Jarnot, R. F., Manney, G. L. and Waters, J. W.: Validation
865 of middle-atmosphere carbon monoxide retrievals from the Microwave Limb Sounder on Aura, J. Geophys. Res. Atmos., 112(D24), doi:10.1029/2007JD008723, 2007.

Qie, X., Wu, X., Yuan, T., Bian, J. and Lu, D.: Comprehensive Pattern of Deep Convective Systems over the Tibetan Plateau–South Asian Monsoon Region Based on TRMM Data, J. Clim.,
870 27(17), 6612–6626, doi:10.1175/JCLI-D-14-00076.1, 2014.

Randel, W. J. and Park, M.: Deep convective influence on the Asian summer monsoon anticyclone and associated tracer variability observed with Atmospheric Infrared Sounder (AIRS), J. Geophys. Res. Atmos., 111(D12), doi:10.1029/2005JD006490, 2006.
875

Santee, M. L., Manney, G. L., Livesey, N. J., Schwartz, M. J., Neu, J. L. and Read, W. G.: A comprehensive overview of the climatological composition of the Asian summer monsoon anticyclone based on 10 years of Aura Microwave Limb Sounder measurements, J. Geophys. Res. Atmos., 122(10), 5491–5514, doi:10.1002/2016JD026408, 2017.
880

Sellitto, P., Sèze, G. and Legras, B.: Secondary sulphate aerosols and cirrus clouds detection with SEVIRI during Nabro volcano eruption, Int. J. Remote Sens., 38(20), 5657–5672, doi:10.1080/01431161.2017.1348635, 2017.

885 Sindelarova, K., Granier, C., Bouarar, I., Guenther, A., Tilmes, S., Stavrakou, T., Müller, J.-F., Kuhn, U., Stefani, P. and Knorr, W.: Global data set of biogenic VOC emissions calculated by the MEGAN model over the last 30 years, Atmos. Chem. Phys., 14(17), 9317–9341, doi:10.5194/acp-14-9317-2014, 2014.

890   Stroppiana, D., Brivio, P. A., Grégoire, J.-M., Liousse, C., Guillaume, B., Granier, C., Mieville, A., Chin, M. and Pétron, G.: Comparison of global inventories of CO emissions from biomass burning derived from remotely sensed data, Atmos. Chem. Phys., 10(24), 12173–12189, doi:10.5194/acp-10-12173-2010, 2010.

895   Sun, J., Zhang, M. and Liu, T.: Spatial and temporal characteristics of dust storms in China and its surrounding regions, 1960–1999: Relations to source area and climate, J. Geophys. Res. Atmos., 106(D10), 10325–10333, doi:10.1029/2000JD900665, 2001.

       Tansey, K., Grégoire, J.-M., Defourny, P., Leigh, R., Pekel, J.-F., van Bogaert, E. and Bartholomé,
900   E.: A new, global, multi-annual (2000–2007) burnt area product at 1 km resolution, Geophys. Res. Lett., 35(1), doi:10.1029/2007GL031567, 2008.

       Thomason, L. W. and Vernier, J.-P.: Improved SAGE II cloud/aerosol categorization and observations of the Asian tropopause aerosol layer: 1989-2005, Atmos. Chem. Phys., 13(9),
905   4605–4616, doi:10.5194/acp-13-4605-2013, 2013.

       Tissier, A.-S. and Legras, B.: Convective sources of trajectories traversing the tropical tropopause layer, Atmos. Chem. Phys., 16, 3383–3398, https://doi.org/10.5194/acp-16-3383-2016, 2016.
910
       van Marle, M. J. E., Kloster, S., Magi, B. I., Marlon, J. R., Daniau, A.-L., Field, R. D., Arneth, A., Forrest, M., Hantson, S., Kehrwald, N. M., Knorr, W., Lasslop, G., Li, F., Mangeon, S., Yue, C., Kaiser, J. W. and van der Werf, G. R.: Historic global biomass burning emissions for CMIP6 (BB4CMIP) based on merging satellite observations with proxies and fire models (1750--2015),
915   Geosci. Model Dev., 10(9), 3329–3357, doi:10.5194/gmd-10-3329-2017, 2017.

       van der Werf, G. R., Randerson, J. T., Giglio, L., van Leeuwen, T. T., Chen, Y., Rogers, B. M., Mu, M., van Marle, M. J. E., Morton, D. C., Collatz, G. J., Yokelson, R. J., and Kasibhatla, P. S.: Global fire emissions estimates during 1997–2016, Earth Syst. Sci. Data, 9, 697–720,
920   https://doi.org/10.5194/essd-9-697-2017, 2017.

       Vernier, J.-P., Thomason, L. W. and Kar, J.: CALIPSO detection of an Asian tropopause aerosol layer, Geophys. Res. Lett., 38(7), doi:10.1029/2010GL046614, 2011.

925   Vernier, J.-P., Fairlie, T. D., Natarajan, M., Wienhold, F. G., Bian, J., Martinsson, B. G., Crumeyrolle, S., Thomason, L. W. and Bedka, K. M.: Increase in upper tropospheric and lower stratospheric aerosol levels and its potential connection with Asian pollution, J. Geophys. Res., 120(4), 1608–1619, doi:10.1002/2014JD022372, 2015.

930   Vernier, H., Wienhold, F. G., Liu, H., Knepp, T. N., Thomason, L., Crawford, J., Ziemba, L., Moore,
J., Crumeyrolle, S., Williamson, M., Berthet, G., Jégou, F. and Renard, J.-B.: BATAL: The Balloon
Measurement Campaigns of the Asian Tropopause Aerosol Layer, Bull. Am. Meteorol. Soc.,
99(5), 955–973, doi:10.1175/BAMS-D-17-0014.1, 2018.

935   Vogel, B., Günther, G., Müller, R., Grooß, J.-U. and Riese, M.: Impact of different Asian source
regions on the composition of the Asian monsoon anticyclone and of the extratropical
lowermost stratosphere, Atmos. Chem. Phys., 15(23), 13699–13716,   doi:10.5194/acp-15-
13699-2015, 2015.

940   Wang, H., Easter, R. C., Rasch, P. J., Wang, M., Liu, X., Ghan, S. J., Qian, Y., Yoon, J.-H., Ma, P.-L.
and Vinoj, V.: Sensitivity of remote aerosol distributions to representation of cloud–aerosol
interactions in a global climate model, Geosci. Model Dev., 6(3), 765–782, doi:10.5194/gmd-6-
765-2013, 2013.

945   Waters, J. W., Froidevaux, L., Harwood, R. S., Jarnot, R. F., Pickett, H. M., Read, W. G., Siegel, P.
H., Cofield, R. E., Filipiak, M. J., Flower, D. A., Holden, J. R., Lau, G. K., Livesey, N. J., Manney, G.
L., Pumphrey, H. C., Santee, M. L., Wu, D. L., Cuddy, D. T., Lay, R. R., Loo, M. S., Perun, V. S.,
Schwartz, M. J., Stek, P. C., Thurstans, R. P., Boyles, M. A., Chandra, K. M., Chavez, M. C., Gun-
Shing Chen, Chudasama, B. V, Dodge, R., Fuller, R. A., Girard, M. A., Jiang, J. H., Yibo Jiang,
950   Knosp, B. W., LaBelle, R. C., Lam, J. C., Lee, K. A., Miller, D., Oswald, J. E., Patel, N. C., Pukala, D.
M., Quintero, O., Scaff, D. M., Van Snyder, W., Tope, M. C., Wagner, P. A. and Walch, M. J.: The
Earth observing system microwave limb sounder (EOS MLS) on the aura Satellite, IEEE Trans.
Geosci. Remote Sens., 44(5), 1075–1092, doi:10.1109/TGRS.2006.873771, 2006.

955   Wei, W., Zhang, R., Yang, S., Li, W., & Wen, M. Quasi-biweekly oscillation of the South Asian
high and its role in connecting the Indian and East Asian summer rainfalls. Geophys. Res. Lett.,
46, 14742-14750. https://doi.org/10.1029/2019GL086180, 2019.

        Wu, C., Lin, Z., Liu, X., Li, Y., Lu, Z. and Wu, M.: Can Climate Models Reproduce the Decadal
960   Change of Dust Aerosol in East Asia?, Geophys. Res. Lett., 45(18), 9953–9962,
doi:10.1029/2018GL079376, 2018.
        Xu, C., Ma, Y. M., You, C. and Zhu, Z. K.: The regional distribution characteristics of aerosol
optical depth over the Tibetan Plateau, Atmos. Chem. Phys., 15(20), 12065–12078,
doi:10.5194/acp-15-12065-2015, 2015.

965

        Yu, P., Toon, O. B., Neely, R. R., Martinsson, B. G. and Brenninkmeijer, C. A. M.: Composition
and physical properties of the Asian Tropopause Aerosol Layer and the North American
Tropospheric   Aerosol   Layer,   Geophys.   Res.   Lett.,   42(7),   2540–2546,
doi:10.1002/2015GL063181, 2015.

970

Yu, P., Rosenlof, K. H., Liu, S., Telg, H., Thornberry, T. D., Rollins, A. W., Portmann, R. W., Bai, Z., Ray, E. A., Duan, Y., Pan, L. L., Toon, O. B., Bian, J. and Gao, R.-S.: Efficient transport of tropospheric aerosol into the stratosphere via the Asian summer monsoon anticyclone, Proc Nati Acad Sci USA, 114(27), 6972–6977, doi:10.1073/pnas.1701170114, 2017.

975

Yuan, C., Lau, W. K. M., Li, Z. and Cribb, M.: Relationship between Asian monsoon strength and transport of surface aerosols to the Asian Tropopause Aerosol Layer (ATAL): interannual variability and decadal changes, Atmos. Chem. Phys., 19(3), 1901–1913, doi:10.5194/acp-19-1901-2019, 2019.

980

Zender, C. S., Bian, H. and Newman, D.: Mineral Dust Entrainment and Deposition (DEAD) model: Description and 1990s dust climatology, J. Geophys. Res. Atmos., 108(D14), doi:10.1029/2002JD002775, 2003.

985

990

995